

Geophysical Research Letters®

RESEARCH LETTER

10.1029/2024GL112467

Key Points:

- Drivers of wet-bulb temperature extremes (WTEs) are analyzed in a pan-African, 10-year convection-permitting model simulation
- Most WTEs are <2,000 km² through combining positive soil moisture anomalies (SMA) locally with warmer and moister large-scale conditions
- SMA-induced mesoscale circulations on scales of 10s km amplify WTEs locally through subsidence and suppressed boundary layer growth

Supporting Information:

Supporting Information may be found in the online version of this article.

Correspondence to:

G. Chagnaud,
guicha@ceh.ac.uk

Citation:

Chagnaud, G., Taylor, C. M., Jackson, L. S., Birch, C. E., Marsham, J. H., & Klein, C. (2025). Wet-bulb temperature extremes locally amplified by wet soils. *Geophysical Research Letters*, 52, e2024GL112467. <https://doi.org/10.1029/2024GL112467>

Received 10 SEP 2024

Accepted 31 MAR 2025

Author Contributions:

Conceptualization: C. M. Taylor, C. E. Birch

Data curation: G. Chagnaud

Formal analysis: G. Chagnaud

Funding acquisition: C. M. Taylor, C. E. Birch

Investigation: G. Chagnaud, L. S. Jackson, C. Klein

Methodology: G. Chagnaud, C. M. Taylor, L. S. Jackson, C. E. Birch, J. H. Marsham

Project administration: C. E. Birch

Supervision: C. M. Taylor







Writing – original draft: G. Chagnaud

Writing – review & editing: G. Chagnaud, C. M. Taylor, L. S. Jackson, C. E. Birch, J. H. Marsham, C. Klein

© 2025. The Author(s).

This is an open access article under the terms of the [Creative Commons Attribution License](https://creativecommons.org/licenses/by/4.0/), which permits use, distribution and reproduction in any medium, provided the original work is properly cited.

Wet-Bulb Temperature Extremes Locally Amplified by Wet Soils

G. Chagnaud¹ , C. M. Taylor^{1,2} , L. S. Jackson³ , C. E. Birch³ , J. H. Marsham^{3,4} , and C. Klein¹ 

¹UK Centre for Ecology and Hydrology, Wallingford, UK, ²National Center for Earth Observation, Wallingford, UK,

³School of Earth and Environment, University of Leeds, Leeds, UK, ⁴Met Office, Exeter, UK

Abstract Wet-bulb temperature extremes (WTEs) occur due to a combination of high humidity and temperature, and are hazardous to human health. Alongside favourable large-scale conditions, surface fluxes play an important role in WTEs; yet, little is known about how land surface heterogeneity influences them. Using a 10-year, pan-African convection-permitting model simulation, we find that most WTEs have spatial extents <2,000 km². They occur preferentially over positive soil moisture anomalies (SMA) typically following rainfall. The wet-bulb temperature is locally amplified by 0.5–0.6°C in events associated with smaller-scale SMA (50 km across) compared to events with larger-scale SMA (300 km across). A mesoscale circulation, resulting from stronger spatial contrasts of sensible heat flux, more efficiently concentrates moist, warm air in a shallower boundary layer. This mechanism could explain the underestimation of peak Twb values in coarser-resolution products. The role of antecedent SMA from recent rainfall may help issue localized early warnings.

Plain Language Summary Heat stress can have harmful consequences for people and ecosystems. Through less effective sweating, ambient air humidity increases the human heat stress. Extreme heat stress occurs when high humidity and temperature associated with large-scale weather patterns combine with surface fluxes of heat and moisture. Current weather and climate models are used to project future heat stress, but cannot represent soil moisture variability on fine spatial scales. Here we investigate the causes of humid heat extremes and quantify the role of soil moisture over the continent of Africa in a high-resolution climate model simulation. Most events are found to occur on spatial scales less than 2,000 km² and to be strongly associated with wet soils from recent rainfall. Wet soils evaporate more moisture into the atmosphere whilst reducing the near-surface mixing of air. This latter factor causes hot, humid air to build up more efficiently near the ground. This study shows that accurately monitoring and forecasting humid heat extremes requires high-resolution data sets where aspects such as wet soil patches from recent rainfall are realistically depicted. It also suggests the potential for early warning of heat stress using near-real-time observations of wet soil or land surface temperature from satellites and weather stations.

1. Introduction

In recent years, heat stress has received increased attention from the climate science community (Barriopedro et al., 2023; Marx et al., 2021) and it is well established that ambient air humidity contributes to heat stress through its limiting effect on the efficiency of sweating, the body's main cooling mechanism (Baldwin et al., 2023; Buzan & Huber, 2020; Matthews, 2018; Sherwood & Huber, 2010). Wet-bulb temperature (Twb) has been widely used to document extreme humid heat for the recent past (Ivanovich et al., 2022, 2024; Justine et al., 2023; Mishra et al., 2020; Raymond et al., 2017, 2021; Rogers et al., 2021; Speizer et al., 2022) and in future climate projections (Birch et al., 2022; Coffel et al., 2018; Freychet et al., 2022; Kang, 2018; Pal & Eltahir, 2016; Schwingshackl et al., 2021; Vecellio et al., 2023; Wang et al., 2021). Wet-bulb temperature extremes (WTEs) result from a combination of physical processes acting at various time and space scales. While the advection of warm, moist air can create favourable conditions (Monteiro & Caballero, 2019; Raymond et al., 2021), a mechanism that limits the mixing of near-surface air with the upper atmospheric layers is also key in WTEs. On the one hand, large-scale subsidence is found over WTEs in the global Tropics (Raymond et al., 2021): this keeps the mid-troposphere dry, thus limiting deep convection and allowing high near-surface Twb values to be reached (Duan et al., 2024). On the other hand, Monteiro and Caballero (2019), Krakauer et al. (2020), and Mishra et al. (2020) find larger peak Twb values associated with enhanced evapotranspiration resulting from wetter soils typically linked to irrigation; increased evapotranspiration not only moistens the boundary layer but also reduces its growth, thus concentrating

hot humid air in a shallower boundary layer (Justine et al., 2023; Mishra et al., 2020). This mechanism is especially effective where soil moisture exerts a strong control on the partitioning of available energy (solar radiation) into surface sensible heat (SH) and latent heat (LH) fluxes. Kong and Huber (2023) indeed find a significant link between wetter soils and higher wet-bulb temperatures in locations broadly corresponding to regions of strong land-atmosphere coupling (Hsu & Dirmeyer, 2022; Koster et al., 2004).

Soil moisture patches due to for example, irrigation or rainfall, can range in size from a few kilometers to tens of kilometers. Therefore, the spatial heterogeneity of land surface evaporative features may not be resolved well in coarse resolution weather and climate models (Coffel et al., 2018; Taylor et al., 2013), eventually affecting the atmospheric state. Taken together, the role of soil moisture in Twb extremes and its rough spatial representation may be one reason for the underestimation of peak Twb values in most gridded climate products, as suggested by some of the above-mentioned studies. In particular, the pan-African study of Birch et al. (2022) reports an underestimate of peak Twb values intensity and frequency in the Met Office Unified Model run at 25 km horizontal grid spacing with parameterized convection (P25) compared to its 4 km, convection-permitting (CP) counterpart. Furthermore, in a future climate simulation under a socio-economic trajectory without policy-driven emissions mitigation (RCP8.5), WTEs are 1.3°C more intense and 30 days yr⁻¹ more frequent by the end of the century in the CP model compared to P25.

Convection-permitting models offer an improved representation of the atmospheric water cycle in general and convection in particular (Birch et al., 2014; Finney et al., 2019; Kendon et al., 2019). Land-atmosphere interactions are also better captured (e.g., the soil moisture-precipitation feedback; Taylor et al., 2013; Hohenegger et al., 2009; Lee & Hohenegger, 2024) thus leading to more heterogeneous and realistic soil moisture and surface flux patterns. Here, we use the same CP model simulation as Birch et al. (2022) to examine the small-scale processes that contribute to WTEs. We first quantify the characteristics and drivers of WTEs. Then, we investigate the relationship between soil moisture and WTE intensity, with an emphasis on the soil moisture length scale effect and the role of land surface-boundary layer coupling.

2. Data and Methods

2.1. Data

The CP4-Africa (CP4A) simulation, performed in the framework of the Improving Model Processes for African Climate (IMPALA) project, is based on the Met Office regional model used for operational weather forecasting (UKV, Tang et al., 2013). The simulation spans the 1997–2006 period and covers the African continent (25°W–57°E, 45°S–40°N) at horizontal grid spacing ranging from 4.4 km at the Equator to 3.2 km at 45°S. The lateral boundary conditions are provided by the global atmospheric simulation performed with the Global Atmosphere 7.0 configuration of the Unified Model (Walters et al., 2019). For a full description of the experimental setup and model evaluation, the reader is referred to Stratton et al. (2018) and Kendon et al. (2019).

Soil moisture is initialized with climatological data derived from an offline simulation of the JULES land surface model (Best et al., 2011), ensuring the spin-up of the four soil layers of the model (the top layer is 10 cm deep). JULES represents the exchanges of energy, mass, and momentum between the surface and the atmosphere, along with surface and sub-surface transfers of water and heat. The surface is represented by 9 surface “tiles” (5 vegetated and 4 non-vegetated), each with its own energy balance, with tile fractional coverage prescribed from land cover mapping. In CP4A, the soil type and associated physical properties were prescribed as sand throughout the domain in order to suppress spurious atmospheric variability created by unrealistic soil texture mapping.

2.2. Method

2.2.1. Sampling Procedure and Study Regions

Among the various heat stress metrics defined in the scientific literature (Buzan et al., 2015; Schwingshackl et al., 2021; Sherwood, 2018), the wet-bulb temperature has been widely used in the climate science community for its physical grounding; we use this metric and discuss some implications of this choice in Section 4. Our WTE sampling procedure goes as follows:

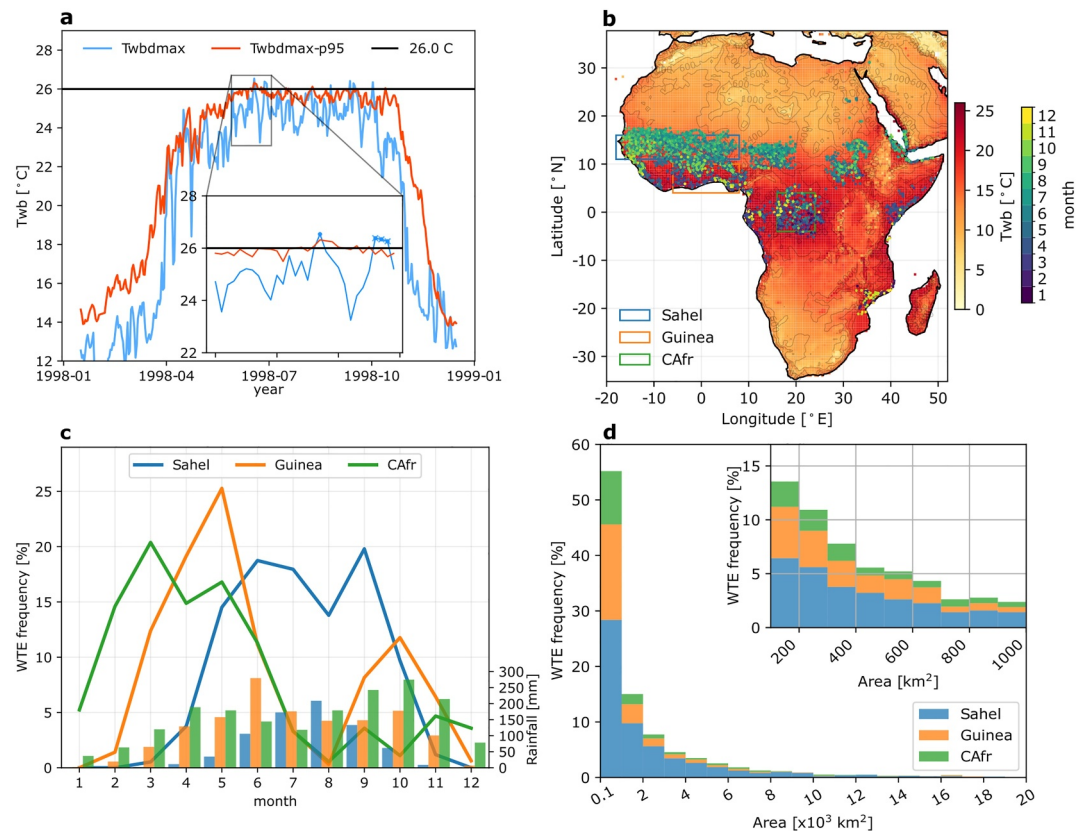


Figure 1. (a) Time series of daily maximum Twb (Twbdmax, blue) and 95th percentile of Twbdmax (Twbdmax-p95, red) for a particular grid cell of CP4A (13.5°N, 2.2°E) and a specific year (1998); a hot-humid day (June 17, dot) and a 3-day sequence thereof (June 26, 27, 28; dots and crosses) are shown in the inset. The 26°C threshold is shown with the horizontal black line. (b) Map of the 1997–2006 climatological mean daily Twb (shading). Dots correspond to the wet-bulb temperature extremes identified over Africa during the 1997–2006 period, with the color denoting the month of occurrence (see right colorbar). (c) Annual distribution of the WTE frequency (%) (solid lines) and monthly cumulative rainfall (mm, vertical bars) for each region. (d) Frequency distribution (in % of the total number of events) of WTEs mean area for 1,000 km² (100 km²) bins in the range 100–20,000 km² (100–1,000 km², inset).

1. Twb is calculated at each grid point from hourly near-surface dry-bulb temperature (T), near-surface specific humidity (q), and surface pressure (p) using the Davies-Jones formula (Davies-Jones, 2008).
2. Because exposure to heat stress over several hours affects health (Sherwood & Huber, 2010; Vanos et al., 2023), the 6-hr running mean of Twb values is calculated and daily maxima of the running mean (denoted Twbdmax) are extracted.

Days that meet the two following criteria are qualified as “hot-humid”:

1. Twbdmax $\geq 26^{\circ}\text{C}$ (black horizontal line in Figure 1a),
2. Twbdmax $\geq 95^{\text{th}}$ percentile of Twbdmax (Twbdmax-p95, red line in Figure 1a). Twbdmax-p95 values are obtained by computing at each grid point, and for each calendar day, the 95th percentile of the Twbdmax values based on a 31-day window centered on this day and aggregated over 10 years (for a total of 310 values). In order to avoid the pitfall evidenced by Brunner and Voigt (2024), the seasonal cycle of Twbdmax is removed prior to the percentile computation.

Clusters of three hot-humid days or more over a contiguous area >5 grid cells ($\approx 100 \text{ km}^2$), identified with a latitude-longitude-time connected components algorithm (see e.g., Vogel et al., 2020), are considered a WTE. Using an absolute threshold of Twb gives the WTEs some degree of physiological relevance: Twb of 35°C is considered the theoretical upper limit for human thermoregulation (Sherwood & Huber, 2010), but serious health impacts have been shown empirically to occur well below this value (Vanos et al., 2023; Vecellio et al., 2022).

The running-window, percentile-based threshold is used to reflect the fact that the experimented heat stress and its consequences also depend on how unusual it is at a given location and time of year.

We focus our analysis on the West African Sahel (11°–16°N, 18°W–8°E, referred to as Sahel thereafter), Guinea (4°–10°N, 6°W–8°E), and Central Africa (CAfr, 4°S–4°N, 16°–24°E), the 3 climatic regions with the largest number of events, although other regions of WTEs exist, mainly located in low-lying and/or coastal areas (Figure 1b). Considering these three regions allows for the spanning of a range of climatic regimes, from the moist equatorial rainforests of Central Africa to the arid environment at the southern fringe of the Sahara desert.

2.2.2. Composite Analysis and Significance Assessment

For each identified event, a $4^\circ \times 4^\circ$ area and a 6-day window centered on the location and day (day0), respectively, of the peak Twb_{dmax} value of the event are considered. This procedure allows to sample the large-scale conditions associated with extreme Twb values. For a given variable x , the hourly climatology \bar{x} is calculated for all grid points and time steps within the space-time composite window using an 11-day running mean from 10 years of data. The anomaly x' is calculated as a departure from this climatology, $x' = x - \bar{x}$. The significance of the anomaly is assessed by comparing x' to a reduced climatology based on the other 9 years of data using a Mann-Whitney test.

3. Results

3.1. Wet-Bulb Temperature Extremes in CP4A

Out of the ~5,300 events identified over the pan-African domain (Figures 1b), 1,515 are in the Sahel (29% of the total population), 637 are in Guinea (12%), and 364 are in Central Africa (7%). Sahelian WTEs are found to occur preferentially during the monsoon season (June–September), with peaks in June and September (Figure 1c). Guinea has a stronger bimodal seasonal cycle with a primary peak in May and a secondary peak in October, thus also in phase with the rainy seasons. In Central Africa, most WTEs occur between February and May that is, prior to and during the first rainy season.

In all regions, WTEs are dominated by short-lived (Figure S1a in Supporting Information S1) and small-scale events: 70% of WTEs have a mean area $<2,000 \text{ km}^2$ and 14% are in the $100\text{--}200 \text{ km}^2$ range (Figure 1d). For reference, a grid cell of the ERA5 reanalysis in the Tropics covers $\approx 650 \text{ km}^2$; grid cells of regional and high-resolution global climate models are about 400 km^2 and $2,500 \text{ km}^2$, respectively. This study thus largely deals with WTEs that would occur at the sub-grid scale in many climate products, and may often be missed by in situ observational networks.

We examine the typical spatial structure of WTEs by compositing events in the 3 regions, centered on the location of the WTE maximum Twb value and sampled on day0. At 1900 local time (LT); the most frequent time of peak Twb values, Figure S1b in Supporting Information S1, an elliptical Twb anomaly (Twb') structure is found in the Sahel (Figure 2a) and to a lesser extent in Guinea (Figure 2e). A more circular pattern of high Twb' is found in Central Africa (Figure 2i). In all cases there is a local Twb amplification: averaged within a radius of 25 km of the center point (circles in Figures 2a–2i), Twb' values are of $1.4\text{--}2.4^\circ\text{C}$ whereas the composite-window average Twb' is of $0.8\text{--}1^\circ\text{C}$.

The pattern of near-surface specific humidity anomalies also displays strong spatial variability in the three regions. There is a local enhancement of $2.2\text{--}3.8 \text{ g kg}^{-1}$ whereas the large-scale averages are in the $0.9\text{--}1.2 \text{ g kg}^{-1}$ range (Figures 2b, 2f, and 2j). The picture is more contrasted when looking at the near-surface dry-bulb temperature anomaly (T'): in the Sahel, there is a significant negative T' of -0.2°C at the 50 km length scale, whereas the composite domain is on average 0.3°C warmer than usual (Figure 2c). In Central Africa, there are positive T' values at both the local and large scales (Figure 2h). This is also the case in Guinea, although T' is slightly negative over the composite-window center point. In the Sahel and Guinea, the increase in q more than offsets the increase in T , leading to an increase in relative humidity (RH) of 1%–12% at all scales over the 6-day period—RH' respectively peaks at +12% and +6.6% at 1900 LT on day0 (Figures S2a and S2b in Supporting Information S1). In Central Africa, RH decreases by 1%–6% at the large-scale; at the local-scale, it oscillates between positive anomalies during nighttime and negative anomalies during daytime, with a local minimum of -4.5% at 1300 LT on day0 (Figure S2d in Supporting Information S1).

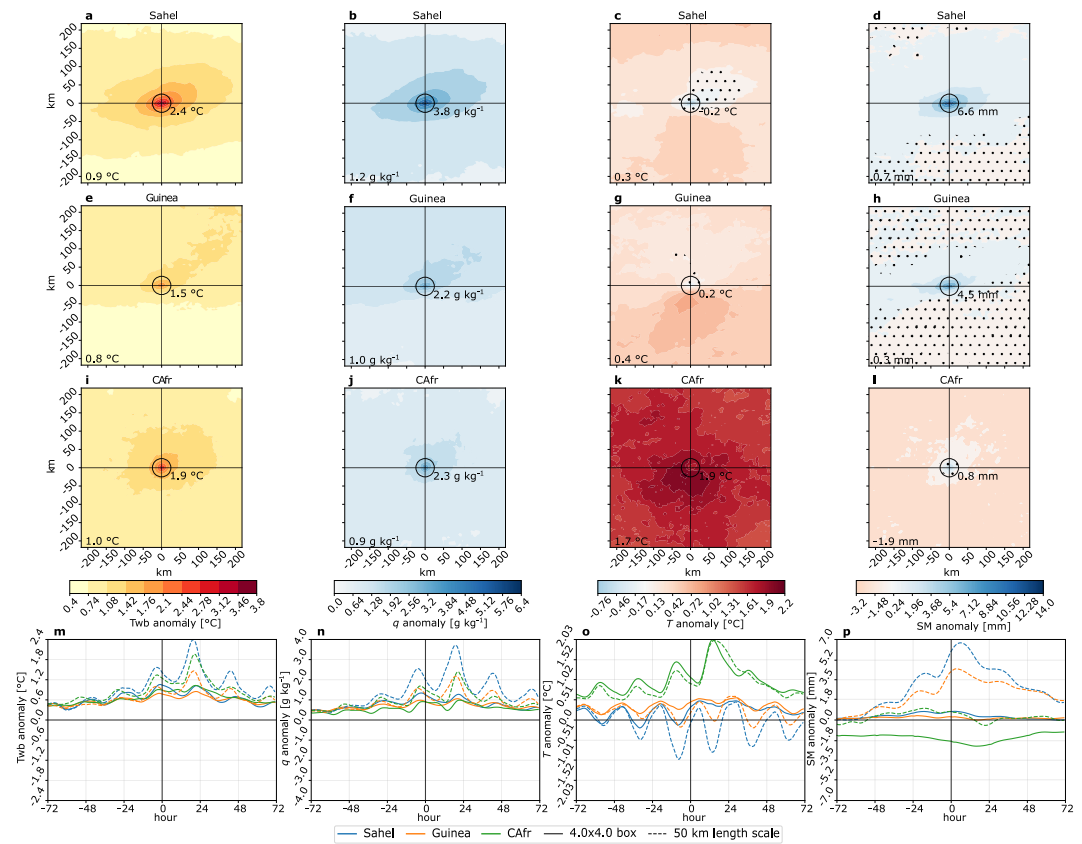


Figure 2. Composite-mean spatial field of Twb (a, e, i), q (b, f, j), and T (c, g, k) anomalies at 1900 LT for the Sahel (a–c), Guinea (e–g), and Central Africa (i–k). Composite-mean spatial field of the 0000–0600 LT average top layer soil moisture anomaly for the Sahel (d), Guinea (h), and Central Africa (l). Values averaged on a 50 km length scale (circle) and the whole composite-window are displayed in the center and the bottom left corner, respectively, of each panel. Locations where the anomaly is not significant at the 1% level or lower are stippled. Composite-mean time series of Twb' (m), q' (n), T' (o) and SMA (p) for the three study regions (color lines, see legend). Spatial averages over the $4 \times 4^\circ$ window and a 50 km length scale are displayed with solid and dashed lines, respectively.

The composite-mean time series of Twb' illustrate not only the local amplification by comparing the local-scale averages (dashed lines) with their large-scale counterparts (solid lines), but also that at large-scale, a positive Twb' of 0.5–1°C prevails over the entire 6-day period (Figure 2m). This is associated with favourable synoptic conditions, with air moister than usual by 0.5–1.25 g kg^{-1} (Figure 2n), bearing in mind that these domain-averaged values encompass the local contribution. Comparison of the spatiotemporal pattern of Twb' and q' shown in Figure 2 highlights the key influence of an additional local source of moisture on WTEs.

3.2. Soil Moisture Control on Wet-Bulb Temperature Extremes

In CP4A, anomalous humidity patterns associated with WTEs are driven by locally wetter soils (Figure 2). In the Sahel and Guinea, top layer soil moisture anomalies (SMA) of 6.6 and 4.5 mm, respectively, are found when averaging within 25 km of the WTE maximum over the first 6 hr of day0. This SMA is highly significant (p value $\leq 1\%$) up to 50–300 km away from the center point, whereas there is little or no significant SMA further North and South (stippled area in Figures 2d and 2h). In Central Africa, there is a smaller but still significant positive SMA of 0.8 mm, peaking at 1.1 mm in the first 6 hr of day-1 (Figure 2p). However, unlike in the other two regions, this positive SMA is surrounded by significantly drier soils (Figures 2i and 2p).

In short, local WTEs occur within anomalously warmer and moister large-scale atmospheric conditions above wet soils whatever the background climatology (shown in Figure S3 in Supporting Information S1). The quasi-elliptical shape of the composite-mean SMA spatial field in the Sahel and Guinea exhibits the classic shape and size of soil moisture anomalies in the aftermath of west/south-westward propagating mesoscale convective

systems (Figures S4a and S4b in Supporting Information S1; see Taylor et al., 2024). In Central Africa, isolated rain cells (Figure S4c in Supporting Information S1) that occur during a generally dry and hot period may explain the spatial pattern shown in Figure 2l.

SMA generate significant surface sensible and latent heat flux anomalies, also displaying strong spatial variability in the three regions (Figure S5 in Supporting Information S1). These anomalies are especially prominent in the Sahel, locally reaching -49 W m^{-2} and 73 W m^{-2} when averaged from 0600 LT to 1800 LT on day0, respectively (heat fluxes are positive upward). Moreover, there is a clear correspondence between the latent (sensible) heat flux pattern across the composite window and the humidity (temperature) structure displayed in Figure 2.

3.3. Effect of Soil Moisture Anomaly Length Scale on Wet-Bulb Temperature Extremes

The preference for WTEs at fine spatial scales (Figure 1d) and the close relationship between Twb' and SMA suggest that soil moisture patterns at fine spatial scales can amplify WTEs. We investigate whether there is a SMA length scale effect on WTEs by looking separately at events associated with smaller- and larger-scale SMA features: we select the events that have the largest antecedent (0000–0600 LT on day0) SMA contrast between a circular area at two length scales—50 and 300 km across (hatched areas in Figures 3a and 3b, respectively)—and the surroundings (excluding the central area; details on this sampling procedure are provided in Text S1 in Supporting Information S1). The resulting SMALL and LARGE samples, respectively, have 123 independent events each. The analysis is restricted to the Sahel region, where most WTEs are identified and where the Twb anomalies are the largest. Only events occurring between May and September are selected (Text S1 in Supporting Information S1).

Figures 3c and 3d show the composite-mean Twb anomaly in SMALL (Twb'_S) and LARGE (Twb'_L), respectively, at 1900 LT (the time when the difference between Twb'_S and Twb'_L is maximum, Figure 3e). Averaging across events on a 50 km length scale, Twb'_S is 2.8°C and Twb'_L is 2.3°C . Extending this analysis to a range of averaging length scales from 10 to 400 km across, Twb'_S is significantly (at the 1% level according to a two-sided Welch's test) larger by $0.5\text{--}0.6^\circ\text{C}$ than Twb'_L up to ≈ 60 km across (Figure 3f). Therefore, in CP4A, smaller-scale SMA features are associated with locally larger-amplitude WTEs. Then, one may wonder whether there is a land surface-atmosphere pathway that filters out the most locally intense WTEs. To address this question, we next look at the coupling between the land surface and the atmosphere in SMALL and LARGE events.

3.4. Land Surface-Induced Mesoscale Circulation

The sensible heat flux is strongly reduced during WTEs, with a sharper spatial contrast in SMALL compared to LARGE (Figures 4a and 4b). At 1500 LT, sensible heat flux anomalies respectively reach -107 W m^{-2} and -73 W m^{-2} when averaged on a 50 km length scale. Spatial contrasts of soil moisture-induced sensible heat flux anomalies are known to drive mesoscale circulations on length scales a few tens of kilometers across in semi-arid environments (Ookouchi et al., 1984; Taylor et al., 2007; Weaver, 2004). An anomalous near-surface divergent flow is clearly distinguishable over the wet feature in SMALL (Figure 4a), with a maximum horizontal wind speed anomaly $U'_S{}^{\text{max}} = 1.1 \text{ m s}^{-1}$. There is also divergence in LARGE, but it is more diffuse ($U'_L{}^{\text{max}} = 0.76 \text{ m s}^{-1}$) and extends over a larger area in response to weaker spatial gradients of sensible heat flux.

The subsiding branch of this circulation is clearly evident in the composite-mean West–East vertical cross-section at 1500 LT on day0 for SMALL, with a coherent descent extending down to 950 hPa (Figure 4c). In contrast, anomalous vertical circulation is not seen in LARGE (Figure 4d). Furthermore, the line plot on the right side of Figure 4c (Figure 4d) shows that, in SMALL (LARGE), the potential wet-bulb temperature anomaly decreases from 2.6°C (2°C) at the surface to 0.8°C (1°C) at 950 hPa, to 0.4°C (0.7°C) at 925 hPa. The stronger vertical gradient of potential wet-bulb temperature in SMALL results from reduced mixing between the surface and the upper levels. This is evidenced by a reduction in the mean boundary layer height of 36 hPa (≈ 370 m) in SMALL WTEs (dashed purple lines in Figure 4c) compared to a reduction of 24 hPa (≈ 245 m) only in LARGE WTEs (Figure 4d), with respect to their climatological counterpart (solid purple lines in Figures 4c and 4d).

This analysis of land surface–boundary layer coupling during WTEs demonstrates that stronger spatial contrasts of sensible heat fluxes resulting from smaller-scale SMA features generate a mesoscale circulation; the subsiding branch of the circulation helps to limit the boundary layer depth and, in so doing, more efficiently concentrates

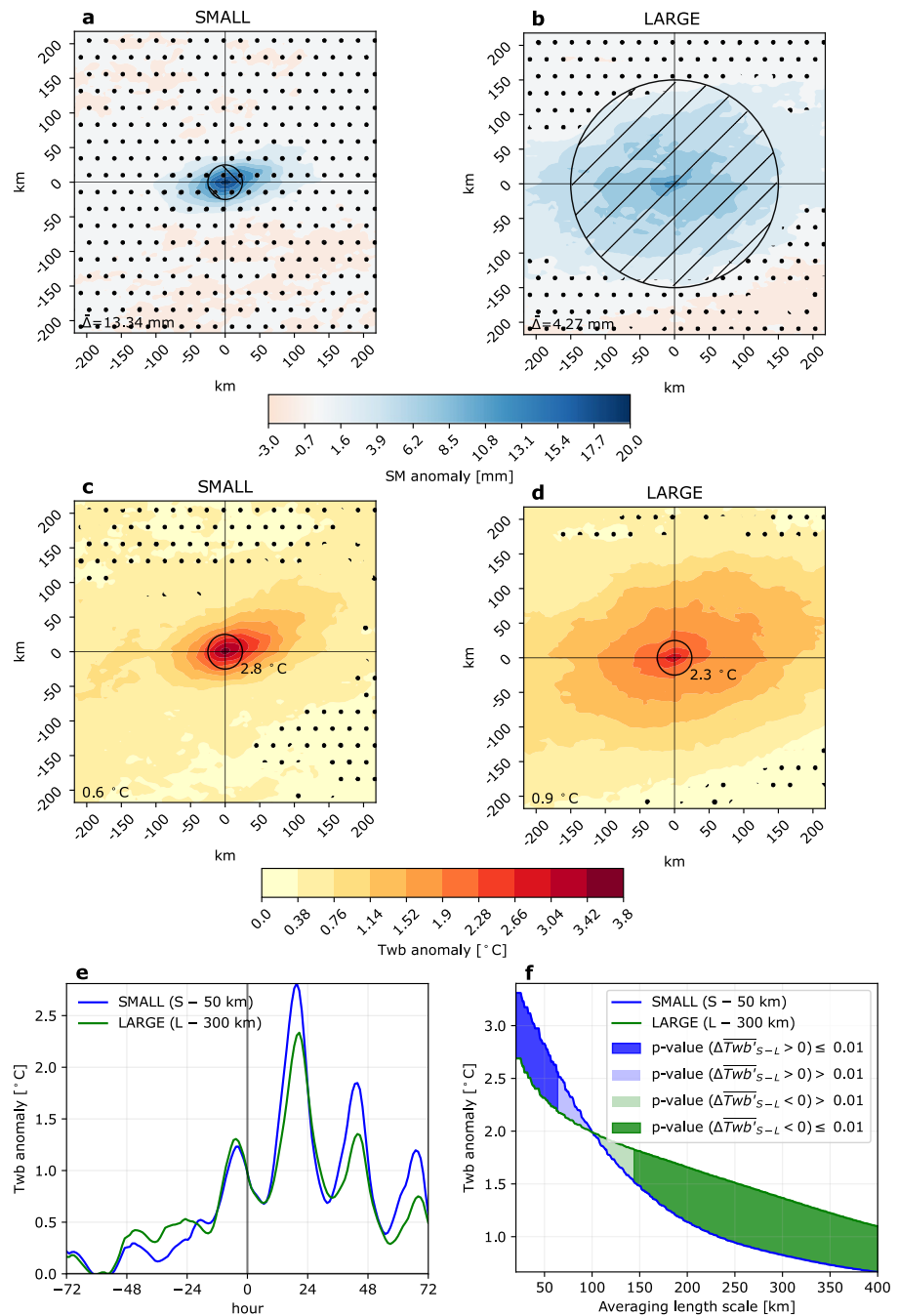


Figure 3. Composite-mean spatial field of antecedent SMA for (a) SMALL and (b) LARGE samples (see Text S1 in Supporting Information S1 for definition; the hatched area corresponds to the averaging area used to discriminate between SMALL and LARGE events). The stippling denotes SMA not significant at the 1% level. Numbers in the bottom left corner indicate the composite-mean SMA contrast (difference between the inner area and the surroundings, denoted Δ). Composite-mean spatial field of Twb' at 1900 LT for (c) SMALL and (d) LARGE. (e) Composite-mean time series of Twb' averaged on a 50 km length scale for SMALL (blue) and LARGE (green) samples. (f) 1900 LT mean Twb' across SMALL ($\overline{Twb'}_S$, blue) and LARGE ($\overline{Twb'}_L$, green) events as a function of averaging length scale, ranging from 10 to 400 km across. The dark blue shading indicates that the difference between $\overline{Twb'}_S$ and $\overline{Twb'}_L$, $\Delta \overline{Twb'}_{S-L}$ is significantly positive (at the 1% level). The dark green shading indicates that $\Delta \overline{Twb'}_{S-L}$ is significantly negative. Light shadings indicate that the two samples of $\overline{Twb'}_S$ and $\overline{Twb'}_L$ values are not significantly different.

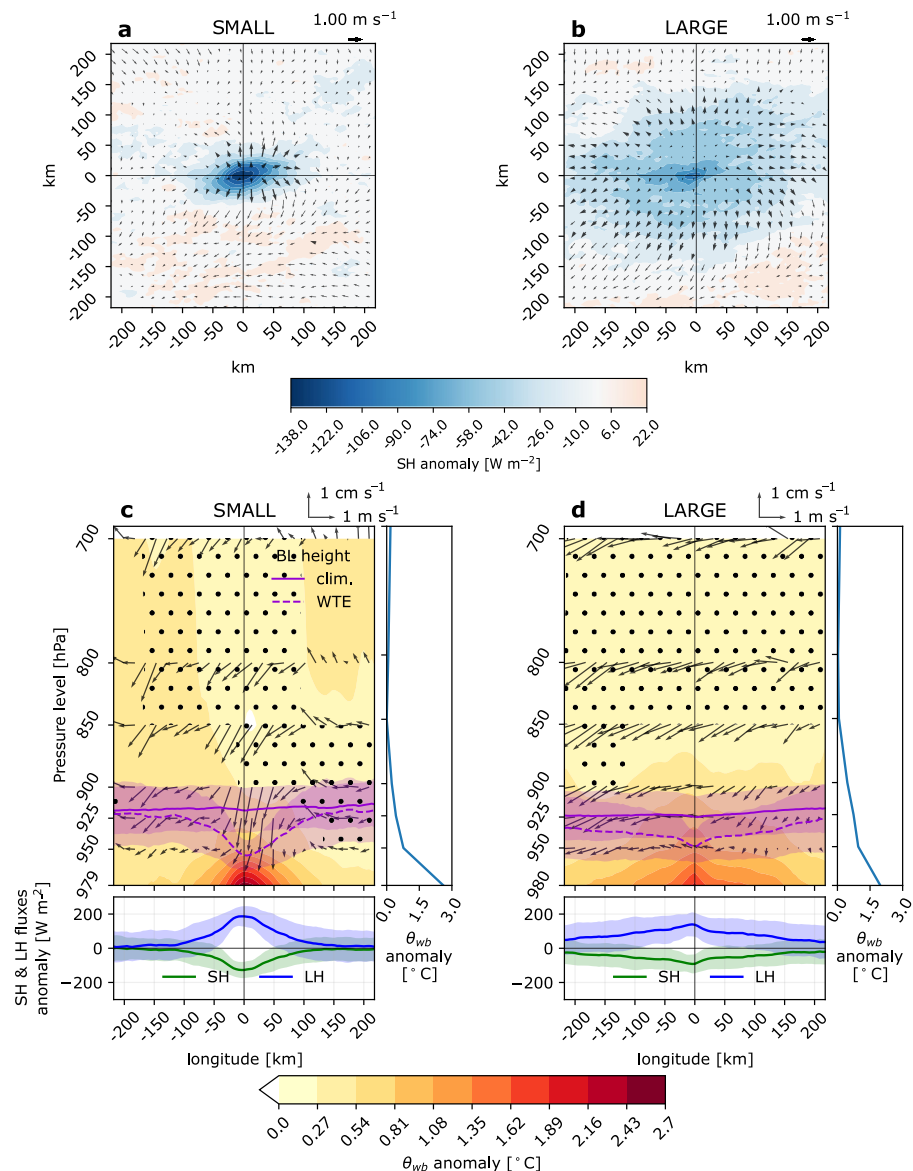


Figure 4. Composite-mean spatial field of 1500 LT sensible heat flux (shading) and 10-m wind (vectors) anomalies in (a) SMALL and (b) LARGE samples. Wind vectors are bold where the sensible heat flux anomaly is significant at the 1% level. West–East vertical cross-section of the composite-mean potential wet-bulb temperature (θ_{wb} in °C, shading) and wind speed (vector scale in the upper right corner) anomalies at 1500 LT interpolated between available pressure levels in (c) SMALL and (d) LARGE samples. Stippling denotes θ_{wb}' with pvalue > 1%. The composite-mean boundary layer height values for climatology and WTEs are shown with purple solid and dashed lines, respectively. The bottom panel displays the sensible (green) and latent (blue) heat flux anomalies across the West–East transect. All shadings around the lines indicate ± 1 standard deviation across events. The right panel shows the vertical profile of θ_{wb}' above the composite window center-point (vertical line in the central panels).

anomalously humid air—resulting from enhanced local evapotranspiration during the day (Figure S6 in Supporting Information S1)—above the wet soil, thereby amplifying peak Twb daytime values.

4. Discussion and Conclusion

Wet-bulb temperature extremes have been systematically analyzed for the first time in a continental scale, convection-permitting climate simulation. The majority of events are found to have spatial extents <2,000 km², meaning that they would be 1–2 grid cells only in products with horizontal grid spacing of 30–40 km. Indeed, a

much larger number of (small-scale) WTEs are found in CP4A compared to both ERA5 and P25 (Text S2 and Figure S7 in Supporting Information S1), where only 7% and 12% of events, respectively, are $<2,000 \text{ km}^2$. The implications for urban heat risk mapping are especially high given that African cities generally have a spatial extent smaller than $2,000 \text{ km}^2$ (e.g., the metropolitan area of Dakar is 535 km^2 and that of Lagos is $1,200 \text{ km}^2$; <https://www.citypopulation.de>).

WTEs are associated with positive antecedent soil moisture anomalies typically following rainfall, confirming the key role of increased evapotranspiration from a wetter land surface in these events (Kong & Huber, 2023; Monteiro & Caballero, 2019). We show how the spatiotemporal pattern of soil moisture–Twb linkage results from the complex, region-dependent interplay between T and q at large-scale, antecedent rainfall at the meso- to local-scale, and the resulting spatiotemporal pattern of soil moisture. Furthermore, we find that smaller-scale soil moisture anomaly features (50 km across) lead to local peak Twb values $0.5\text{--}0.6^\circ\text{C}$ larger compared to larger-scale SMA features (300 km across). This study thus highlights the need for high spatial resolution data sets in which the spatial heterogeneity of transient land surface states and fluxes is captured well to monitor and predict WTEs accurately.

The local amplification is the result of a mesoscale circulation developing in response to sharper spatial contrasts of sensible heat flux. The descending branch of this circulation, located above wet soils, concentrates more efficiently near-surface air with high moisture content in a very shallow boundary layer. These processes are dominant in regions of strong land-atmosphere coupling typically found in semi-arid environments (South-eastern US, the Sahel, North-western India, Northern Australia; Hsu & Dirmeyer, 2022; Koster et al., 2004), where strong spatial contrasts of rainfall-induced soil moisture and turbulent heat fluxes are expected. The amplifying mechanism therefore probably acts beyond Africa, in regions where near-surface Twb is highly sensitive to soil moisture variability (see Kong & Huber, 2023, their Figure 6). In addition, irrigation applied at small spatial scales would also create mesoscale sensible heat flux contrasts and evapotranspiration hotspots, potentially triggering and amplifying WTEs. The role of the thermally-driven mesoscale circulation on WTEs complements the finding of Raymond et al. (2021); Duan et al. (2023), who identified large-scale subsidence as a key “top-down” controlling mechanism of WTEs in the world’s most hot-humid regions. However, contrary to large-scale atmospheric drivers of humid heat extremes, the mesoscale “bottom-up” mechanism identified here may only be captured in products with a sufficiently small horizontal grid spacing—typically $\mathcal{O}(1\text{--}10 \text{ km})$ —explicitly resolving convection (Hohenegger et al., 2015; Taylor et al., 2013).

This study is based on a simulation of the coupled land-atmosphere system using a single model. Each land scheme simulates the response of evapotranspiration to soil moisture differently (Gallego-Elvira et al., 2019) with, for example, different thresholds determining the balance between water-limited and energy-limited evapotranspiration. A direct read-across of SMA–WTE behaviour in any specific region from CP4A to the real world should therefore be made with caution. However, data currently being processed indicate that the SMA–WTE relationship behaves similarly in other regions of the world and/or with other models (Figures S8–S10 in Supporting Information S1). On the other hand, observations in diverse semi-arid regions show that SMA-induced mesoscale circulations play an important role in convective initiation (Barton et al., 2020; Chug et al., 2023; Taylor et al., 2011). Here we have shown how such circulations also have an impact in amplifying WTEs locally. We can therefore be confident in stating that where strong soil moisture heterogeneity influences evapotranspiration (whether from antecedent rainfall, irrigation, or inland water bodies), the mesoscale atmospheric response will strengthen the WTE resulting from favourable large-scale conditions. Furthermore, we expect this effect to be strongest for wet patches on length scales a few tens of kilometers, where the patch center is influenced by edge effects. Idealized simulations will provide more insight into the effects of the SMA length scale on WTEs in various environments.

The use of Twb as an indicator of heat stress also deserves to be discussed. Compared to other heat stress metrics, Twb is more sensitive to changes in q than to changes in T , especially at high T (Sherwood, 2018; Simpson et al., 2023). A sensitivity analysis carried out with the Heat Index (HI, see Text S3 in Supporting Information S1) shows that HI-based extremes are largely associated with increased T , reduced q , and dry soil anomalies (Figure S11 in Supporting Information S1). Nonetheless, putting WTEs in their HI context, on average 73% and 26% of WTEs, respectively, are found to belong to the Extreme Caution ($\text{HI} \in [33\text{--}40^\circ\text{C}]$) and Danger ($\text{HI} \in [41\text{--}51^\circ\text{C}]$) categories of the US National Weather Service classification. Therefore, the “moist” heat extremes identified here with a q -sensitive metric ($\text{RH} > 60\%$ and $T \in [27\text{--}34^\circ\text{C}]$ in most cases; Figure S12 in Supporting Information S1)

are also heat extremes from the point of view of a heat stress metric whose relative sensitivity to T and q is more balanced. The health implications of humid heat stress, which vary between regions and seasons due to different thermal regimes (e.g., warm-humid vs. hot-dry; Vecellio et al., 2022), remain highly uncertain and dependent on the metric used (Baldwin et al., 2023; Lu & Roms, 2023).

A large proportion of the world's population is located in the Tropics and subtropics, where heat-related hazards are already the highest and are projected to increase the most (Dajuma et al., 2024; Freychet et al., 2022; Im et al., 2017; Rogers et al., 2021; Schwingshackl et al., 2021; Vecellio et al., 2023). These regions may also be very vulnerable to heat stress due to limited adaptive capacity—little access to (drinking) water, electricity, and healthcare—and the predominance of outdoor activities (e.g., farming and herding). The need for adaptation strategies to the increasing risk of heat stress is thus critical there. Soil moisture anomalies from recent rainfall are observable on daily and subdaily timescales at high spatial resolution (e.g., Yin et al., 2020); this would allow meteorologists to issue localized hazard alerts at lead times of hours to a day. This information may prove useful and actionable as part of the early warning system for heat advocated by Brimicombe et al. (2024).

Data Availability Statement

CP4A and P25 data are available on JASMIN, the UK's collaborative data analysis environment (<https://www.jasmin.ac.uk>). ERA5 data are available from the Copernicus Climate Change Service (C3S) Climate Data Store (CDS) at Hersbach et al. (2023). CONUS404 data are available from the NSF NCAR Research Data Archive at Rasmussen, Liu, et al. (2023). This work also used resources from the Deutsches Klimarechenzentrum (DKRZ) granted by its Scientific Steering Committee (WLA) under project ID1153. The Python code used to compute wet-bulb temperature is available at https://github.com/cr2630git/wetbulb_dj08_spedup. The codes used to process the data and plot the figures are available at Chagnaud (2025).

Acknowledgments

The authors thank the anonymous reviewers for their constructive comments that helped improve the clarity of the paper. They also thank Colin Raymond and Rob Warren for the Python implementation of the Davies-Jones formula for the calculation of wet-bulb temperature, and William Silversmith for the connected components algorithm (<https://pypi.org/project/connected-components-3d/>). The authors acknowledge the Met Office and Rachel Stratton in particular for the CP4A simulation. The authors are grateful to James Done (NSF NCAR) and Cathy Hohenegger (MPI-met) for stimulating discussions on this work and for providing access to the CONUS404 and ICON data, respectively. This work was supported by the NERC (Grants NE/X013618/1 and NE/X013596/1).

References

- Baldwin, J. W., Benmarhnia, T., Ebi, K. L., Jay, O., Lutsko, N. J., & Vanos, J. K. (2023). Humidity's role in heat-related health outcomes: A heated debate. *Environmental Health Perspectives*, 131(5), 055001. <https://doi.org/10.1289/EHP11807>
- Barriopedro, D., García-Herrera, R., Ordóñez, C., Miralles, D. G., & Salcedo-Sanz, S. (2023). Heat waves: Physical understanding and scientific challenges. *Reviews of Geophysics*, 61(2), e2022RG000780. <https://doi.org/10.1029/2022RG000780>
- Barton, E. J., Taylor, C. M., Parker, D. J., Turner, A. G., Belušić, D., Böing, S. J., et al. (2020). A case-study of land-atmosphere coupling during monsoon onset in northern India. *Quarterly Journal of the Royal Meteorological Society*, 146(731), 2891–2905. <https://doi.org/10.1002/qj.3538>
- Best, M. J., Pryor, M., Clark, D. B., Rooney, G. G., Essery, R. L. H., Ménard, C. B., et al. (2011). The joint UK Land Environment Simulator (JULES), model description—Part 1: Energy and water fluxes. *Geoscientific Model Development*, 4(3), 677–699. <https://doi.org/10.5194/gmd-4-677-2011>
- Birch, C. E., Jackson, L. S., Finney, D. L., Marsham, J. M., Stratton, R. A., Tucker, S., et al. (2022). Future changes in African heatwaves and their drivers at the convective scale. *Journal of Climate*, 35(18), 5981–6006. <https://doi.org/10.1175/jcli-d-21-0790.1>
- Birch, C. E., Parker, D. J., Marsham, J. H., Copsey, D., & García-Carreras, L. (2014). A seamless assessment of the role of convection in the water cycle of the West African Monsoon. *Journal of Geophysical Research: Atmospheres*, 119(6), 2890–2912. <https://doi.org/10.1002/2013JD020887>
- Brimicombe, C., Runkle, J. D., Tuholske, C., Domeisen, D. I. V., Gao, C., Toftum, J., & Otto, I. M. (2024). Preventing heat-related deaths: The urgent need for a global early warning system for heat. *PLOS Climate*, 3(7), e0000437. <https://doi.org/10.1371/journal.pclm.0000437>
- Brunner, L., & Voigt, A. (2024). Pitfalls in diagnosing temperature extremes. *Nature Communications*, 15(1), 2087. <https://doi.org/10.1038/s41467-024-46349-x>
- Buzan, J. R., & Huber, M. (2020). Moist heat stress on a hotter Earth. *Annual Review of Earth and Planetary Sciences*, 48(1), 623–655. <https://doi.org/10.1146/annurev-earth-053018-060100>
- Buzan, J. R., Oleson, K., & Huber, M. (2015). Implementation and comparison of a suite of heat stress metrics within the Community Land Model version 4.5. *Geoscientific Model Development*, 8(2), 151–170. <https://doi.org/10.5194/gmd-8-151-2015>
- Chagnaud, G. (2025). guichag/H2X: H2X [Software]. Zenodo. <https://doi.org/10.5281/zenodo.14785052>
- Chug, D., Dominguez, F., Taylor, C. M., Klein, C., & Nesbitt, S. W. (2023). Dry-to-wet soil gradients enhance convection and rainfall over subtropical South America. *Journal of Hydrometeorology*, 24(9), 1563–1581. <https://doi.org/10.1175/JHM-D-23-0031.1>
- Coffel, E. D., Horton, R. M., & De Sherbinin, A. (2018). Temperature and humidity based projections of a rapid rise in global heat stress exposure during the 21st century. *Environmental Research Letters*, 13(1), 014001. <https://doi.org/10.1088/1748-9326/aaa00e>
- Dajuma, A., Sylla, M. B., Tall, M., Almazroui, M., Afiesimama, E., Dosio, A., et al. (2024). Projected intensification and expansion of heat stress and related population exposure over Africa under future climates. *Earth's Future*, 12(12), e2024EF004646. <https://doi.org/10.1029/2024EF004646>
- Davies-Jones, R. (2008). An efficient and accurate method for computing the wet-bulb temperature along pseudoadiabats. *Monthly Weather Review*, 136(7), 2764–2785. <https://doi.org/10.1175/2007MWR2224.1>
- Duan, S. Q., Ahmed, F., & Neelin, J. D. (2024). Moist heatwaves intensified by entrainment of dry air that limits deep convection. *Nature Geoscience*, 17(9), 837–844. <https://doi.org/10.1038/s41561-024-01498-y>
- Duan, S. Q., Findell, K. L., & Fueglistaler, S. A. (2023). Coherent mechanistic patterns of tropical land hydroclimate changes. *Geophysical Research Letters*, 50(7), e2022GL102285. <https://doi.org/10.1029/2022GL102285>

- Finney, D. L., Marsham, J. H., Jackson, L. S., Kendon, E. J., Rowell, D. P., Boorman, P. M., et al. (2019). Implications of improved representation of convection for the East Africa water budget using a convection-permitting model. *Journal of Climate*, 32(7), 2109–2129. <https://doi.org/10.1175/JCLI-D-18-0387.1>
- Freychet, N., Hegerl, G. C., Lord, N. S., Lo, Y. T. E., Mitchell, D., & Collins, M. (2022). Robust increase in population exposure to heat stress with increasing global warming. *Environmental Research Letters*, 17(6), 064049. <https://doi.org/10.1088/1748-9326/ac71b9>
- Gallego-Elvira, B., Taylor, C. M., Harris, P. P., & Ghent, D. (2019). Evaluation of regional-scale soil moisture-surface flux dynamics in Earth system models based on satellite observations of land surface temperature. *Geophysical Research Letters*, 46(10), 5480–5488. <https://doi.org/10.1029/2019GL082962>
- Hersbach, H., Bell, B., Berrisford, P., Biavati, G., Horányi, A., Muñoz Sabater, J., et al. (2023). ERA5 hourly data on single levels from 1940 to present [Dataset]. *Copernicus Climate Change Service (C3S) Climate Data Store (CDS)*. <https://doi.org/10.24381/cds.adbb2d47>
- Hohenegger, C., Brockhaus, P., Bretherton, C. S., & Schär, C. (2009). The soil moisture–precipitation feedback in simulations with explicit and parameterized convection. *Journal of Climate*, 22(19), 5003–5020. <https://doi.org/10.1175/2009JCLI2604.1>
- Hohenegger, C., Schlemmer, L., & Silvers, L. (2015). Coupling of convection and circulation at various resolutions. *Tellus A: Dynamic Meteorology and Oceanography*, 67(1), 26678. <https://doi.org/10.3402/tellusa.v67.26678>
- Hsu, H., & Dirmeyer, P. A. (2022). Deconstructing the soil moisture–latent heat flux relationship: The range of coupling regimes experienced and the presence of nonlinearity within the sensitive regime. *Journal of Hydrometeorology*, 23(7), 1041–1057. <https://doi.org/10.1175/JHM-D-21-0224.1>
- Im, E.-S., Pal, J. S., & Eltahir, E. A. B. (2017). Deadly heat waves projected in the densely populated agricultural regions of South Asia. *Science Advances*, 3(8). <https://doi.org/10.1126/sciadv.1603322>
- Ivanovich, C., Anderson, W., Horton, R., Raymond, C., & Sobel, A. (2022). The influence of Intraseasonal Oscillations on humid heat in the Persian Gulf and South Asia. *Journal of Climate*, 35(13), 4309–4329. <https://doi.org/10.1175/JCLI-D-21-0488.1>
- Ivanovich, C. C., Horton, R. M., Sobel, A. H., & Singh, D. (2024). Subseasonal variability of humid heat during the South Asian Summer Monsoon. *Geophysical Research Letters*, 51(6), e2023GL107382. <https://doi.org/10.1029/2023GL107382>
- Justine, J., Monteiro, J. M., Shah, H., & Rao, N. (2023). The diurnal variation of wet bulb temperatures and exceedance of physiological thresholds relevant to human health in South Asia. *Communications Earth & Environment*, 4(1), 244. <https://doi.org/10.1038/s43247-023-00897-0>
- Kang, S., & Eltahir, E. A. B. (2018). North China Plain threatened by deadly heatwaves due to climate change and irrigation. *Nature Communications*, 9(1), 2894. <https://doi.org/10.1038/s41467-018-05252-y>
- Kendon, E. J., Stratton, R. A., Tucker, S., Marsham, J. H., Berthou, S., Rowell, D. P., & Senior, C. A. (2019). Enhanced future changes in wet and dry extremes over Africa at convection-permitting scale. *Nature Communications*, 10(1), 1794. <https://doi.org/10.1038/s41467-019-09776-9>
- Kong, Q., & Huber, M. (2023). Regimes of soil moisture–wet-bulb temperature coupling with relevance to moist heat stress. *Journal of Climate*, 36(22), 7925–7942. <https://doi.org/10.1175/JCLI-D-23-0132.1>
- Koster, R. D., Dirmeyer, P. A., Guo, Z., Bonan, G., Chan, E., Cox, P., et al. (2004). Regions of strong coupling between soil moisture and precipitation. *Science*, 305(5687), 1138–1140. <https://doi.org/10.1126/science.1100217>
- Krakauer, N. Y., Cook, B. I., & Puma, M. J. (2020). Effect of irrigation on humid heat extremes. *Environmental Research Letters*, 15(9), 094010. <https://doi.org/10.1088/1748-9326/ab9ecf>
- Lee, J., & Hohenegger, C. (2024). Weaker land–atmosphere coupling in global storm-resolving simulation. *Proceedings of the National Academy of Sciences of the United States of America*, 121(12), e2314265121. <https://doi.org/10.1073/pnas.2314265121>
- Lu, Y.-C., & Roms, D. M. (2023). Is a wet-bulb temperature of 35°C the correct threshold for human survivability? *Environmental Research Letters*, 18(9), 094021. <https://doi.org/10.1088/1748-9326/ace83c>
- Marx, W., Haunschild, R., & Bornmann, L. (2021). Heat waves: A hot topic in climate change research. *Theoretical and Applied Climatology*, 146(1), 781–800. <https://doi.org/10.1007/s00704-021-03758-y>
- Matthews, T. (2018). Humid heat and climate change. *Progress in Physical Geography: Earth and Environment*, 42(3), 391–405. <https://doi.org/10.1177/0309133318776490>
- Mishra, V., Ambika, A. K., Asoka, A., Aadhar, S., Buzan, J., Kumar, R., & Huber, M. (2020). Moist heat stress extremes in India enhanced by irrigation. *Nature Geoscience*, 13(11), 722–728. <https://doi.org/10.1038/s41561-020-00650-8>
- Monteiro, J. M., & Caballero, R. (2019). Characterization of extreme wet-bulb temperature events in southern Pakistan. *Geophysical Research Letters*, 46(17–18), 10659–10668. <https://doi.org/10.1029/2019GL084711>
- Ookouchi, Y., Segal, M., Kessler, R. C., & Pielke, R. A. (1984). Evaluation of soil moisture effects on the generation and modification of mesoscale circulations. *Monthly Weather Review*, 112(11), 2281–2292. [https://doi.org/10.1175/1520-0493\(1984\)112<2281:EOSMEO>2.0.CO;2](https://doi.org/10.1175/1520-0493(1984)112<2281:EOSMEO>2.0.CO;2)
- Pal, J. S., & Eltahir, E. A. B. (2016). Future temperature in southwest Asia projected to exceed a threshold for human adaptability. *Nature Climate Change*, 6(2), 197–200. <https://doi.org/10.1038/nclimate2833>
- Rasmussen, R. M., Liu, C., Ikeda, K., Chen, F., Kim, J.-H., Schneider, T., et al. (2023). Four-kilometer long-term regional hydroclimate reanalysis over the conterminous United States (CONUS) [Dataset]. *Research Data Archive at the National Center for Atmospheric Research, Computational and Information Systems Laboratory*. <https://doi.org/10.5065/ZYY0-Y036>
- Raymond, C., Matthews, T., Horton, R. M., Fischer, E. M., Fueglistaler, S., Ivanovich, C., et al. (2021). On the controlling factors for globally extreme humid heat. *Geophysical Research Letters*, 48(23), e2021GL096082. <https://doi.org/10.1029/2021GL096082>
- Raymond, C., Singh, D., & Horton, R. M. (2017). Spatiotemporal patterns and synoptics of extreme wet-bulb temperature in the contiguous United States. *Journal of Geophysical Research: Atmospheres*, 122(24), 13108–13124. <https://doi.org/10.1002/2017JD027140>
- Rogers, C. D. W., Ting, M., Li, C., Kornhuber, K., Coffel, E. D., Horton, R. M., et al. (2021). Recent increases in exposure to extreme humid-heat events disproportionately affect populated regions. *Geophysical Research Letters*, 48(19), e2021GL094183. <https://doi.org/10.1029/2021GL094183>
- Schwingshackl, C., Sillmann, J., Vicedo-Cabrera, A. M., Sandstad, M., & Aunan, K. (2021). Heat stress indicators in CMIP6: Estimating future trends and exceedances of impact-relevant thresholds. *Earth's Future*, 9(3), e2020EF001885. <https://doi.org/10.1029/2020EF001885>
- Sherwood, S. C. (2018). How important is humidity in heat stress? *Journal of Geophysical Research: Atmospheres*, 123(21), 11808–11810. <https://doi.org/10.1029/2018JD028969>
- Sherwood, S. C., & Huber, M. (2010). An adaptability limit to climate change due to heat stress. *Proceedings of the National Academy of Sciences of the United States of America*, 107(21), 9552–9555. <https://doi.org/10.1073/pnas.0913352107>
- Simpson, C. H., Brousse, O., Ebi, K. L., & Heavyside, C. (2023). Commonly used indices disagree about the effect of moisture on heat stress. *npj Climate and Atmospheric Science*, 6(1), 78. <https://doi.org/10.1038/s41612-023-00408-0>
- Speizer, S., Raymond, C., Ivanovich, C., & Horton, R. M. (2022). Concentrated and intensifying humid heat extremes in the IPCC AR6 regions. *Geophysical Research Letters*, 49(5), e2021GL097261. <https://doi.org/10.1029/2021GL097261>

- Stratton, R. A., Senior, C. A., Vosper, S. B., Folwell, S. S., Boutle, I. A., Earnshaw, P. D., et al. (2018). A pan-African convection-permitting regional climate simulation with the Met Office unified model: CP4-Africa. *Journal of Climate*, 31(9), 3485–3508. <https://doi.org/10.1175/JCLI-D-17-0503.1>
- Tang, Y., Lean, H. W., & Bornemann, J. (2013). The benefits of the Met Office variable resolution NWP model for forecasting convection. *Meteorological Applications*, 20(4), 417–426. <https://doi.org/10.1002/met.1300>
- Taylor, C. M., Birch, C. E., Parker, D. J., Dixon, N., Guichard, F., Nikulin, G., & Lister, G. M. S. (2013). Modeling soil moisture-precipitation feedback in the Sahel: Importance of spatial scale versus convective parameterization. *Geophysical Research Letters*, 40(23), 6213–6218. <https://doi.org/10.1002/2013GL058511>
- Taylor, C. M., Gounou, A., Guichard, F., Harris, P. P., Ellis, R. J., Couvreur, F., & De Kauwe, M. (2011). Frequency of Sahelian storm initiation enhanced over mesoscale soil-moisture patterns. *Nature Geoscience*, 4(7), 430–433. <https://doi.org/10.1038/ngeo1173>
- Taylor, C. M., Klein, C., & Harris, B. L. (2024). Multiday soil moisture persistence and atmospheric predictability resulting from Sahelian mesoscale convective systems. *Geophysical Research Letters*, 51(20), e2024GL109709. <https://doi.org/10.1029/2024GL109709>
- Taylor, C. M., Parker, D. J., & Harris, P. P. (2007). An observational case study of mesoscale atmospheric circulations induced by soil moisture. *Geophysical Research Letters*, 34(15), 2007GL030572. <https://doi.org/10.1029/2007GL030572>
- Vanos, J., Guzman-Echavarria, G., Baldwin, J. W., Bongers, C., Ebi, K. L., & Jay, O. (2023). A physiological approach for assessing human survivability and liveability to heat in a changing climate. *Nature Communications*, 14(1), 7653. <https://doi.org/10.1038/s41467-023-43121-5>
- Vecellio, D. J., Kong, Q., Kenney, W. L., & Huber, M. (2023). Greatly enhanced risk to humans as a consequence of empirically determined lower moist heat stress tolerance. *Proceedings of the National Academy of Sciences of the United States of America*, 120(42), e2305427120. <https://doi.org/10.1073/pnas.2305427120>
- Vecellio, D. J., Wolf, S. T., Cottle, R. M., & Kenney, W. L. (2022). Evaluating the 35°C wet-bulb temperature adaptability threshold for young, healthy subjects (PSU HEAT Project). *Journal of Applied Physiology*, 132(2), 340–345. <https://doi.org/10.1152/jappphysiol.00738.2021>
- Vogel, M. M., Zscheischler, J., Fischer, E. M., & Seneviratne, S. I. (2020). Development of future heatwaves for different hazard thresholds. *Journal of Geophysical Research: Atmospheres*, 125(9), e2019JD032070. <https://doi.org/10.1029/2019JD032070>
- Walters, D., Baran, A. J., Boutle, I., Brooks, M., Earnshaw, P., Edwards, J., et al. (2019). The Met Office unified model global atmosphere 7.0/7.1 and JULES global land 7.0 configurations. *Geoscientific Model Development*, 12(5), 1909–1963. <https://doi.org/10.5194/gmd-12-1909-2019>
- Wang, P., Yang, Y., Tang, J., Leung, L. R., & Liao, H. (2021). Intensified humid heat events under global warming. *Geophysical Research Letters*, 48(2), e2020GL091462. <https://doi.org/10.1029/2020GL091462>
- Weaver, C. P. (2004). Coupling between large-scale atmospheric processes and mesoscale land-atmosphere interactions in the U.S. Southern Great Plains during summer. Part II: Mean impacts of the mesoscale. *Journal of Hydrometeorology*, 5(6), 1247–1258. <https://doi.org/10.1175/JHM-397.1>
- Yin, J., Zhan, X., Liu, J., Moradkhani, H., Fang, L., & Walker, J. P. (2020). Near-real-time one-kilometre soil moisture active passive soil moisture data product. *Hydrological Processes*, 34(21), 4083–4096. <https://doi.org/10.1002/hyp.13857>

References From the Supporting Information

- Hersbach, H., Bell, B., Berrisford, P., Hirahara, S., Horányi, A., Muñoz-Sabater, J., et al. (2020). The ERA5 global reanalysis. *Quarterly Journal of the Royal Meteorological Society*, 146(730), 1999–2049. <https://doi.org/10.1002/qj.3803>
- Hohenegger, C., Korn, P., Linardakis, L., Redler, R., Schnur, R., Adamidis, P., et al. (2023). ICON-sapphire: Simulating the components of the Earth system and their interactions at kilometer and subkilometer scales. *Geoscientific Model Development*, 16(2), 779–811. <https://doi.org/10.5194/gmd-16-779-2023>
- Nicholson, S. E. (2013). The West African Sahel: A review of recent studies on the rainfall regime and its interannual variability. *International Scholarly Research Notices*, 2013(1), 453521–453532. (Publisher: Wiley Online Library). <https://doi.org/10.1155/2013/453521>
- Rasmussen, R. M., Chen, F., Liu, C., Ikeda, K., Prein, A., Kim, J., et al. (2023). CONUS404: The NCAR-USGS 4-km long-term regional hydroclimate reanalysis over the CONUS. *Bulletin of the American Meteorological Society*, 104(8), E1382–E1408. <https://doi.org/10.5065/ZYY0-Y036>
- Steadman, R. G. (1979). The assessment of sultriness. Part I: A temperature-humidity index based on human physiology and clothing science. *Journal of Applied Meteorology and Climatology*, 18(7), 861–873. [https://doi.org/10.1175/1520-0450\(1979\)018<0861:TAOSPI>2.0.CO;2](https://doi.org/10.1175/1520-0450(1979)018<0861:TAOSPI>2.0.CO;2)